# Sensitivity curves for searches for gravitational-wave backgrounds

Eric Thrane[1, a] and Joseph D. Romano[2, b]

[1]*LIGO Laboratory, California Institute of Technology, MS 100-36, Pasadena, California 91125, USA*
[2]*Department of Physics and Astronomy and Center for Gravitational-Wave Astronomy,*
*University of Texas at Brownsville, Texas 78520, USA*
(Dated: October 15, 2013)

We propose a graphical representation of detector sensitivity curves for stochastic gravitational-wave backgrounds that takes into account the increase in sensitivity that comes from *integrating over frequency* in addition to integrating over time. This method is valid for backgrounds that have a power-law spectrum in the analysis band. We call these graphs "power-law integrated curves." For simplicity, we consider cross-correlation searches for unpolarized and isotropic Gaussian stochastic backgrounds using two or more detectors. We apply our method to construct power-law integrated sensitivity curves for correlation measurements involving second-generation ground-based detectors such as Advanced LIGO, space-based detectors such as the Big Bang Observer (BBO), and timing residuals from a pulsar timing array. The code used to produce these plots is available at `https://dcc.ligo.org/LIGO-P1300115` for researchers interested in constructing similar sensitivity curves for their analyses.

## I. INTRODUCTION

When discussing the feasibility of detecting gravitational waves using current or planned detectors, one often plots characteristic strain $h_c(f)$ curves of predicted signals, and compares them to *sensitivity* curves for different detectors. The sensitivity curves are usually constructed by taking the ratio of the detector's noise power spectral density $P_n(f)$ to its sky- and polarization-averaged response to a gravitational wave $\mathcal{R}(f)$, defining $S_n(f) \equiv P_n(f)/\mathcal{R}(f)$ and an effective strain noise amplitude $h_n(f) \equiv \sqrt{f S_n(f)}$, which can then be compared to $h_c(f)$. If the curve corresponding to a predicted signal lies above the detector sensitivity curve in some frequency band, then the signal has signal-to-noise ratio $>1$. An example of such a plot is shown in Fig. 1, which is taken from [1].

For stochastic gravitational waves, which are typically searched for by cross-correlating data from two or more detectors, one often adjusts the height of a sensitivity curve to take into account the total observation time (e.g., $T = 1$ yr or 5 yr). For uncorrelated detector noise, the expected squared signal-to-noise ratio of a cross-correlation search for a gravitational-wave background for frequencies between $f$ and $f + \delta f$ scales like $\sqrt{T \delta f}$. So the effective strain noise amplitude $h_n(f)$ should be multiplied by a factor of $1/(T\delta f)^{1/4}$. Also, instead of characteristic strain, one often plots the predicted fractional energy density in gravitational waves $\Omega_{\rm gw}(f)$ as a function of frequency, which is proportional to $f^2 h_c^2(f)$ (see Eq. 6). An example of such a plot is shown in Fig. 2, which is taken from [2].

But for stochastic gravitational waves, plots such as Figs. 1 and 2 do not always tell the full story. Searches
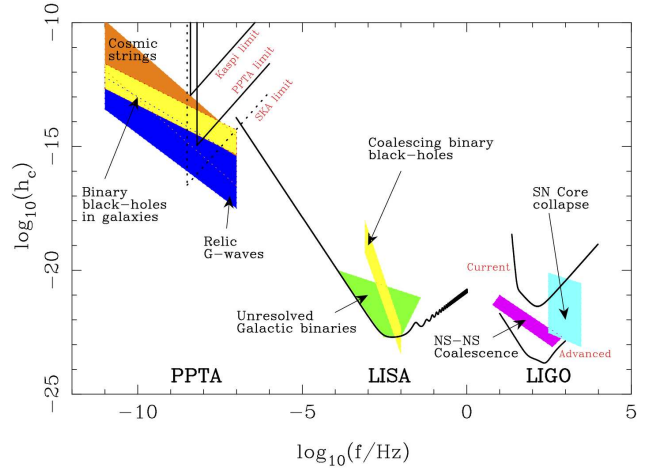


FIG. 1: Sensitivity curves for gravitational-wave observations and the predicted spectra of various gravitational-wave sources, taken from [1].

for gravitational-wave backgrounds also benefit from the *broadband* nature of the signal. The broadband squared signal-to-noise ratio $\rho \equiv \mathrm{SNR}^2$ (see Eq. 21) also scales like $\sqrt{N_{\rm bins}} = \sqrt{\Delta f/\delta f}$, where $N_{\rm bins}$ is the number of frequency bins $\delta f$ in the total bandwidth $\Delta f$. As we shall see below, the actual value of the proportionality constant depends on the spectral shape of the background and on the detector geometry (e.g., the separation and relative orientation of the detectors), in addition to the individual detector noise power spectral densities. Since this improvement to the sensitivity is *signal dependent*, it is not always folded into the detector sensitivity curves [1], even though the improvement in sensitivity can be sig-

---

[a]Electronic address: `ethrane@ligo.caltech.edu`
[b]Electronic address: `joseph.romano@ligo.org`

[1] To be clear, integration over frequency is always carried out in searches for stochastic gravitational-wave backgrounds, even
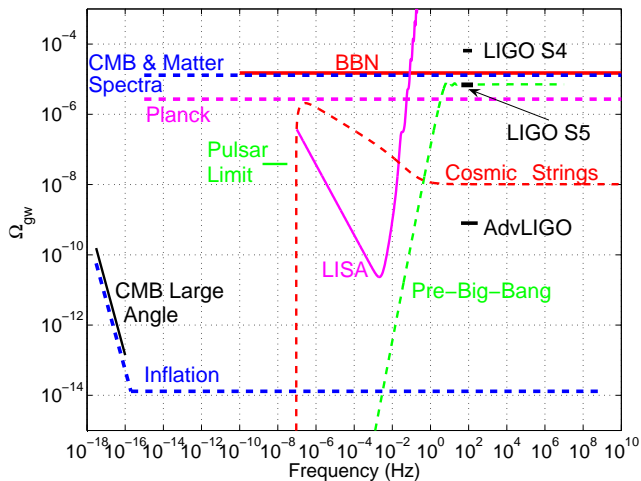
FIG. 2: Plot showing strengths of predicted gravitational-wave backgrounds in terms of $\Omega_{\mathrm{gw}}(f)$ and the corresponding sensitivity curves for different detectors, taken from [2]. Upper limits from various measurements, e.g., S5 LIGO Hanford-LIGO Livingston and pulsar timing, are shown as horizontal lines in the analysis band of each detector. The upper limits take into account integration over frequency, but only for a single spectral index.
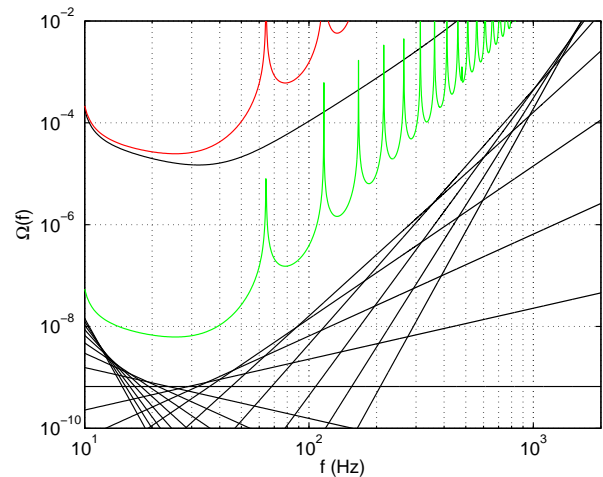


FIG. 3: $\Omega_{\mathrm{gw}}(f)$ sensitivity curves from different stages in a potential future Advanced LIGO Hanford-LIGO Livingston correlation search for power-law gravitational-wave backgrounds. The top black curve is the single-detector sensitivity curve, assumed to be the same for both H1 or L1. The red curve shows the sensitivity of the H1L1 detector pair to a gravitational-wave background, where the spikes are due to zeros in the Hanford-Livingston overlap reduction function (see left panel, Fig. 5). The green curve shows the improvement in sensitivity that comes from integration over an observation time of 1 year for a frequency bin size of 0.25 Hz. The set of black lines are obtained by integrating over frequency for different power law indices, assuming a squared signal-to-noise ratio $\rho = 1$. Finally, the blue power-law integrated sensitivity curve is the envelope of the black lines. See Sec. III, Fig. 7 for more details.

nificant. And when it is folded in, as in Fig 2, a single spectral index is assumed, making it difficult to compare published limits with arbitrary models. In other cases, limits are given as a function of spectral index, but the constrained quantity depends on an arbitrary reference frequency; see Eq. 7.

To illustrate the improvement in sensitivity that comes from integrating over frequency, consider the simple case of a white gravitational-wave background signal in white uncorrelated detector noise. In this case, $\rho$ increases by precisely $\sqrt{N_{\mathrm{bins}}}$ compared to the single bin analysis. For ground-based detectors like LIGO, typical values of $\Delta f$ and $\delta f$ are $\Delta f \approx 100$ Hz and $\delta f \approx 0.25$ Hz, leading to $N_{\mathrm{bins}} \approx 400$, and a corresponding improvement in $\rho$ of about 20. For colored spectra and non-trivial detector geometry the improvement will be less, but a factor of $\sim 5$-$10$ increase in $\rho$ is not unrealistic.

In this paper, we propose a relatively simple way to graphically represent this improvement in sensitivity for gravitational-wave backgrounds that have a *power-law* frequency dependence in the sensitivity band of the detectors. An example of such a "power-law integrated sensitivity curve" is given in Fig. 3 for a correlation measurement between the Advanced LIGO detectors in Hanford, WA and Livingston, LA. Details of the construction and interpretation of these curves will be given in Sec III, Fig. 7. We show this figure now for readers who might be anxious to get to the punchline.

In Sec. II, we briefly review the fundamentals of cross-correlation searches for gravitational-wave backgrounds, defining an effective strain noise power spectral density $S_{\mathrm{eff}}(f)$ for a network of detectors. For simplicity, we consider cross-correlation searches for unpolarized and isotropic Gaussian stochastic backgrounds using two or more detectors. In Sec. III we present a graphical method for constructing sensitivity curves for power-law backgrounds based on the expected squared signal-to-noise ratio for the search, and we apply our method to construct new power-law integrated sensitivity curves for correlation measurements involving second-generation ground-based detectors such as Advanced LIGO, space-based detectors such as the Big Bang Observer (BBO), and a pulsar timing array. We conclude with a brief discussion in Sec. IV.

## II. FORMALISM

In this section, we summarize the fundamental properties of a stochastic gravitational-wave background and the correlated response of a network of detectors to such a background. In order to keep track of the many different variables necessary for this discussion, we have included

though this is not always depicted in sensitivity curves.

Table I, which summarizes key variables.

## A. Statistical properties

In transverse-traceless coordinates, the metric perturbations $h_{ab}(t, \vec{x})$ corresponding to a gravitational-wave background can be written as a linear superposition of sinusoidal plane gravitational waves with frequency $f$, propagation direction $\hat{k}$, and polarization $A$:

$$h_{ab}(t, \vec{x}) = \int_{-\infty}^{\infty} df \int_{S^2} d^2\Omega_{\hat{k}} \sum_A h_A(f, \hat{k}) e_{ab}^A(\hat{k}) e^{i2\pi f(t - \hat{k}\cdot\vec{x}/c)}, \quad (1)$$

where $e_{ab}^A(\hat{k})$ are the gravitational-wave polarization tensors and $A = +, \times$ (see e.g., [3]). The Fourier components $h_A(f, \hat{k})$ are *random* fields whose expectation values define the statistical properties of the background. Without loss of generality we can assume $\langle h_A(f, \hat{k}) \rangle = 0$. For unpolarized, isotropic, and Gaussian stochastic backgrounds, the quadratic expectation values have the form

$$\langle h_A(f, \hat{k}) h_{A'}^*(f', \hat{k}') \rangle = \frac{1}{16\pi} \delta(f - f') \delta_{AA'} \delta^2(\hat{k}, \hat{k}') S_h(f), \quad (2)$$

where

$$S_h(f) = \frac{3H_0^2}{2\pi^2} \frac{\Omega_{\text{gw}}(f)}{f^3} \quad (3)$$

is the gravitational-wave power spectral density, and

$$\Omega_{\text{gw}}(f) = \frac{1}{\rho_c} \frac{d\rho_{\text{gw}}}{d\ln f} \quad (4)$$

is the fractional contribution of the energy density in gravitational waves to the total energy density needed to close the universe [3]. (Throughout this paper we utilize single-sided power spectra.) The variable $\rho_c$ denotes the critical energy density of the universe while $d\rho_{\text{gw}}$ denotes the energy density between $f$ and $f + df$. In terms of the characteristic strain

$$h_c(f) \equiv \sqrt{f S_h(f)}, \quad (5)$$

it follows that

$$\Omega_{\text{gw}}(f) = \frac{2\pi^2}{3H_0^2} f^2 h_c^2(f). \quad (6)$$

## B. Power-law backgrounds

In this paper, we will restrict our attention to gravitational-wave backgrounds that can be described by power-law spectra:

$$\Omega_{\text{gw}}(f) = \Omega_\beta \left( \frac{f}{f_{\text{ref}}} \right)^\beta, \quad (7)$$

where $\beta$ is the spectral index and $f_{\text{ref}}$ is a reference frequency, typically set to $1\,\text{yr}^{-1}$ for pulsar-timing observations and $100\,\text{Hz}$ for ground-based detectors. The choice of $f_{\text{ref}}$, however, is arbitrary and does not affect the detectability of the signal.

It follows trivially that the characteristic strain also has a power-law form:

$$h_c(f) = A_\alpha \left( \frac{f}{f_{\text{ref}}} \right)^\alpha, \quad (8)$$

where the amplitude $A_\alpha$ and spectral index $\alpha$ are related to $\Omega_\beta$ and $\beta$ via:

$$\Omega_\beta = \frac{2\pi^2}{3H_0^2} f_{\text{ref}}^2 A_\alpha^2, \quad \beta = 2\alpha + 2. \quad (9)$$

For inflationary backgrounds relevant for cosmology, it is often assumed that

$$\Omega_{\text{gw}}(f) = \text{const}, \quad (10)$$

for which $\beta = 0$ and $\alpha = -1$. For a background arising from binary coalescence,

$$\Omega_{\text{gw}}(f) \propto f^{2/3}, \quad (11)$$

for which $\beta = 2/3$ and $\alpha = -2/3$. This power-law dependence is applicable to super-massive black-hole coalescences targeted by pulsar timing observations as well as compact binary coalescences relevant for ground-based and space-based detectors.

## C. Detector response

The response $h(t)$ of a detector to a passing gravitational wave is the convolution of the metric perturbations $h_{ab}(t, \vec{x})$ with the impulse response $R^{ab}(t, \vec{x})$:

$$h(t) \equiv \int_{-\infty}^{\infty} d\tau \int d^3y \, R^{ab}(\tau, \vec{y}) h_{ab}(t - \tau, \vec{x} - \vec{y})$$
$$= \int_{-\infty}^{\infty} df \int d^2\Omega_{\hat{k}} \sum_A R^A(f, \hat{k}) h_A(f, \hat{k}) e^{i2\pi f(t - \hat{k}\cdot\vec{x}/c)},$$
$$(12)$$

where $\vec{x}$ is the location of the measurement at time $t$. The function $R^A(f, \hat{k})$ is the detector response to a sinusoidal plane-wave with frequency $f$, propagation direction $\hat{k}$, and polarization $A$. In the frequency domain, we have

$$\tilde{h}(f) = \int d^2\Omega_{\hat{k}} \sum_A R^A(f, \hat{k}) h_A(f, \hat{k}) e^{-i2\pi f \hat{k}\cdot\vec{x}/c}. \quad (13)$$

## D. Overlap reduction function

Given two detectors, labeled by $I$ and $J$, the expectation value of the cross-correlation of the detector responses $\tilde{h}_I(f)$ and $\tilde{h}_J(f)$ is

$$\langle \tilde{h}_I(f) \tilde{h}_J^*(f') \rangle = \frac{1}{2} \delta(f - f') \Gamma_{IJ}(f) S_h(f), \quad (14)$$

| variable | definition |
|---|---|
| $h_{ab}(t, \vec{x})$ | metric perturbation, Eq. 1 |
| $h_A(f, \hat{k})$ | Fourier coefficients of metric perturbation, Eq. 1 |
| $S_h(f)$ | strain power spectral density of a gravitational-wave background, Eq. 3 |
| $\Omega_{\rm gw}(f)$ | fractional energy density spectrum of a gravitational-wave background, Eq. 4 |
| $h_c(f)$ | characteristic strain for gravitational waves, Eq. 5 |
| $h(t)$ | detector response to gravitational waves, Eq. 12 |
| $R_I^A(f, \hat{k})$ | detector response to a sinusoidal plane gravitational wave, Eq. 12 |
| $\tilde{h}(f)$ | Fourier transform of $h(t)$, Eq. 13 |
| $\Gamma_{IJ}(f)$ | overlap reduction function for the correlated response to a gravitational-wave background, Eq. 15 |
| $\mathcal{R}_I(f)$ | detector response to a gravitational wave averaged over polarizations and directions on the sky, Eq. 17 |
| $P_{hI}(f)$ | detector power spectral density due to gravitational waves, Eq. 18 |
| $P_{nI}(f)$ | detector power spectral density due to noise, Eq. 21 |
| $S_{\rm eff}(f)$ | effective strain noise power spectral density for a detector network, Eq. 23 |
| $h_{\rm eff}(f)$ | effective strain noise amplitude for a detector network, Eq. 24 |
| $S_n(f)$ | strain noise power spectral density for a single detector, Eq. 27 |
| $h_n(f)$ | strain noise amplitude for a single detector, $h_n(f) \equiv \sqrt{f S_n(f)}$ |

TABLE I: Summary of select variables with references to key equations.

where

$$\Gamma_{IJ}(f) \equiv$$
$$\frac{1}{8\pi} \int d^2\Omega_{\hat{k}} \sum_A R_I^A(f, \hat{k}) R_J^{A*}(f, \hat{k}) e^{-i2\pi f \hat{k} \cdot (\vec{x}_I - \vec{x}_J)/c} \tag{15}$$

is the *overlap reduction function* (see e.g., [4, 5] in the context of ground-based interferometers). Note that $\Gamma_{IJ}(f)$ is the transfer function between gravitational-wave strain power $S_h(f)$ and detector response cross-power $C_{IJ}(f) = \Gamma_{IJ}(f) S_h(f)$. It is often convenient to define a *normalized* overlap reduction function $\gamma_{IJ}(f)$ such that for two identical, co-located and co-aligned detectors, $\gamma_{IJ}(0) = 1$. For identical interferometers with opening angle $\delta$,

$$\gamma_{IJ}(f) = (5/\sin^2 \delta)\, \Gamma_{IJ}(f). \tag{16}$$

For a single detector (i.e., $I = J$), we define

$$\mathcal{R}_I(f) \equiv \Gamma_{II}(f), \tag{17}$$

which is the transfer function between gravitational-wave strain power $S_h(f)$ and detector response auto power

$$P_{hI}(f) = \mathcal{R}_I(f) S_h(f). \tag{18}$$

Note that $\mathcal{R}_I(f)$ is the antenna pattern of detector $I$ averaged over polarizations and directions on the sky. A plot of $\mathcal{R}_I(f)$ normalized to unity for the strain response of an equal-arm Michelson interferometer is shown in Fig. 4.

Detailed derivations and discussions of the overlap reduction functions for ground-based laser interferometers,
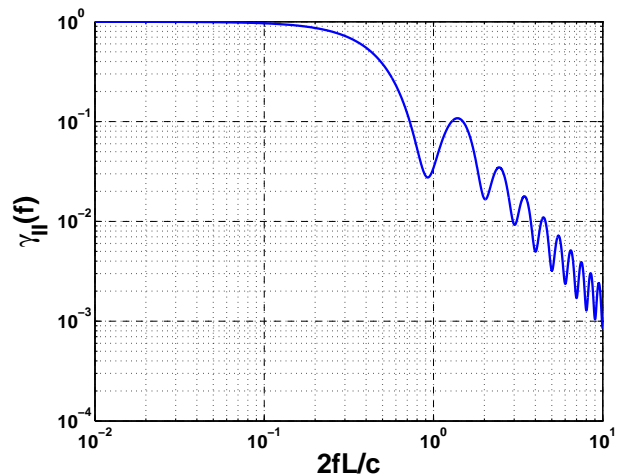


FIG. 4: A plot of the transfer function $\mathcal{R}_I(f) = \gamma_{II}(f)$ normalized to unity for the strain response of an equal-arm Michelson interferometer. The dips in the transfer function occur around integer multiples of $c/(2L)$, where $L$ is the arm length of the interferometer.

space-based laser interferometers, and pulsar timing arrays can be found in [3–5], [6, 7], and [8, 9], respectively. In Fig. 5 we plot the overlap reduction functions for the strain response of the LIGO Hanford-LIGO Livingston detector pair in the long-wavelength limit (valid for frequencies below a few kHz), and the strain response of a pair of mini LISA-like Michelson interferometers in the hexagram configuration of the Big-Bang Observer (BBO), which is a proposed space-based mission, whose goal is the direct detection of the cosmological gravitational-wave background [10–12]. The two

Michelson interferometers for the BBO overlap reduction function are located at opposite vertices of a hexagram ('Star of David') and have arm lengths $L = 5 \times 10^7$ m and opening angles $\delta = 60°$.

In Fig. 6, we plot both the overlap reduction function and the Hellings and Downs curve [8] for the timing response of a pair of pulsars in a pulsar timing array. Assuming the pulsars are separated by an angle $\psi_{IJ}$ on the sky, then to a very good approximation [9]:

$$\Gamma_{IJ}(f) = \frac{1}{(2\pi f)^2} \frac{1}{3} \zeta_{IJ} \qquad (19)$$

where

$$\zeta_{IJ} \equiv \frac{3}{2} \left( \frac{1 - \cos\psi_{IJ}}{2} \right) \log \left( \frac{1 - \cos\psi_{IJ}}{2} \right) - \frac{1}{4} \left( \frac{1 - \cos\psi_{IJ}}{2} \right) + \frac{1}{2} + \frac{1}{2}\delta_{IJ} \qquad (20)$$

is the Hellings and Downs factor [8]. (The normalization is chosen so that for a single pulsar $\zeta_{II} = 1$.)

### E. Signal-to-noise ratio

The expected squared signal-to-noise ratio ($\rho \equiv \mathrm{SNR}^2$) for a cross-correlation search for an unpolarized and isotropic stochastic background is given by [3]:

$$\rho = \sqrt{2T} \left[ \int_0^\infty df \frac{\Gamma_{IJ}^2(f) S_h^2(f)}{P_{nI}(f) P_{nJ}(f)} \right]^{1/2}, \qquad (21)$$

where $T$ is the total (coincident) observation time and $P_{nI}(f)$, $P_{nJ}(f)$ are the auto power spectral densities for the noise in detectors $I$, $J$. This the total *broadband* signal-to-noise ratio, integrated over both time and frequency. It can be derived as the expected signal-to-noise ratio of a filtered cross-correlation of the output of two detectors, where the filter function is chosen so as to maximize the signal-to-noise ratio of the cross-correlation. For a *network* of detectors, this generalizes to

$$\rho = \sqrt{2T} \left[ \int_0^\infty df \sum_{I=1}^{M} \sum_{J>I}^{M} \frac{\Gamma_{IJ}^2(f) S_h^2(f)}{P_{nI}(f) P_{nJ}(f)} \right]^{1/2}, \qquad (22)$$

where $M$ the number of individual detectors, and we have assumed the same coincident observation time $T$ for each detector.

The above expression for $\rho$ suggests the following definition of an *effective* strain noise power spectral density for the detector network

$$S_{\mathrm{eff}}(f) \equiv \left[ \sum_{I=1}^{M} \sum_{J>I}^{M} \frac{\Gamma_{IJ}^2(f)}{P_{nI}(f) P_{nJ}(f)} \right]^{-1/2}, \qquad (23)$$

with corresponding strain noise amplitude

$$h_{\mathrm{eff}}(f) \equiv \sqrt{f S_{\mathrm{eff}}(f)}. \qquad (24)$$

In terms of $S_{\mathrm{eff}}(f)$, we have

$$\rho = \sqrt{2T\delta f} \sqrt{N_{\mathrm{bins}}} \left\langle \frac{S_h^2}{S_{\mathrm{eff}}^2} \right\rangle^{1/2}, \qquad (25)$$

where $\langle \ \rangle$ denotes an average [2] over the total bandwidth of the detectors, $\Delta f = N_{\mathrm{bins}} \delta f$. For the case of $M$ identical, co-located and co-aligned detectors, things simplify further. First,

$$S_{\mathrm{eff}}(f) = \sqrt{\frac{2}{M(M-1)}} \, S_n(f), \qquad (26)$$

where

$$S_n(f) \equiv P_n(f)/\mathcal{R}(f) \qquad (27)$$

is the strain noise power spectral density in a single detector. Second,

$$\rho = \sqrt{T\delta f} \sqrt{N_{\mathrm{bins}}} \sqrt{M(M-1)} \left\langle \frac{S_h^2}{S_n^2} \right\rangle^{1/2}. \qquad (28)$$

Thus, we see that the expected squared signal-to-noise ratio scales linearly with the number of detectors for $M \gg 1$, the square-root of the total observation time, and the square-root of the number of frequency bins. Note that $\sqrt{T\delta f}\sqrt{N_{\mathrm{bins}}} = \sqrt{T\Delta f}$, which is the total time-frequency volume of the measurement.

## III. POWER-LAW INTEGRATED CURVES

### A. Construction

The sensitivity curves that we propose are based on Eq. 22 for the expected squared signal-to-noise ratio $\rho$, applied to gravitational-wave backgrounds with power-law spectra. These "power-law integrated sensitivity curves" include the improvement in sensitivity that comes from the broadband nature of the signal, via the integration over frequency. The following construction is cast in terms of $\Omega_{\mathrm{gw}}(f)$, but we note that power-law integrated curves can also easily be constructed for $h_c(f)$ or $S_h(f)$ using Eqs. 3 and 5 to convert between the different quantities.

1. Begin with the detector noise power spectral densities $P_{nI}(f)$, $P_{nJ}(f)$, and the overlap reduction functions $\Gamma_{IJ}(f)$ for two or more detectors. Using Eq. 23, first calculate the effective strain power spectral density $S_{\mathrm{eff}}(f)$, and then convert it to energy density units $\Omega_{\mathrm{eff}}(f)$ using Eq. 3.

---

[2] Explicitly, $\langle X \rangle \equiv \frac{1}{\Delta f} \int_{f_{\min}}^{f_{\max}} X(f) \, df$
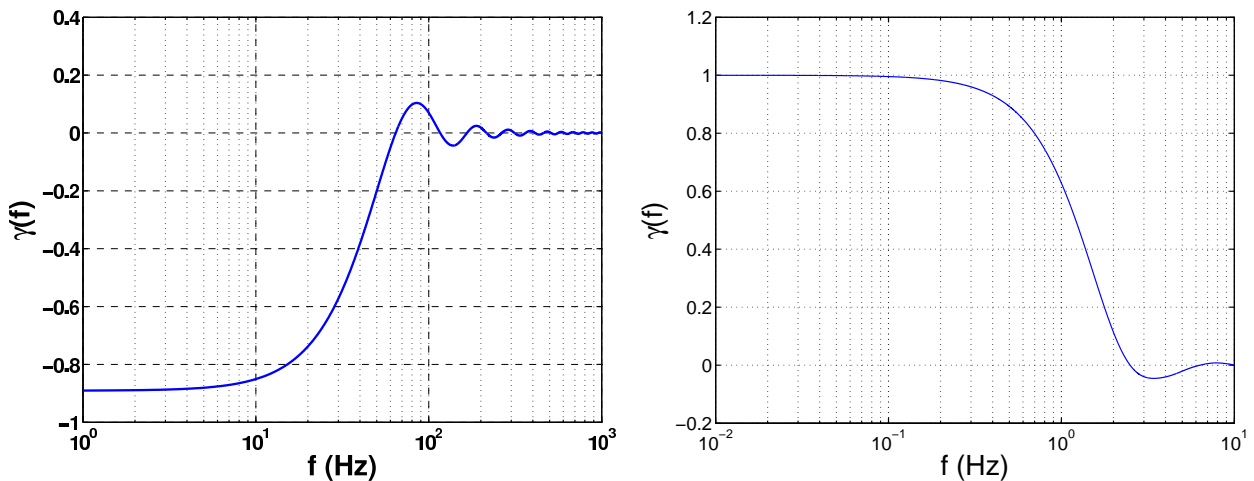
FIG. 5: Left panel: Normalized overlap reduction function for the LIGO detectors located in Hanford, WA and Livingston, LA. Right panel: Normalized overlap reduction function for two mini LISA-like Michelson interferometers located at opposite vertices of the BBO hexagram configuration.
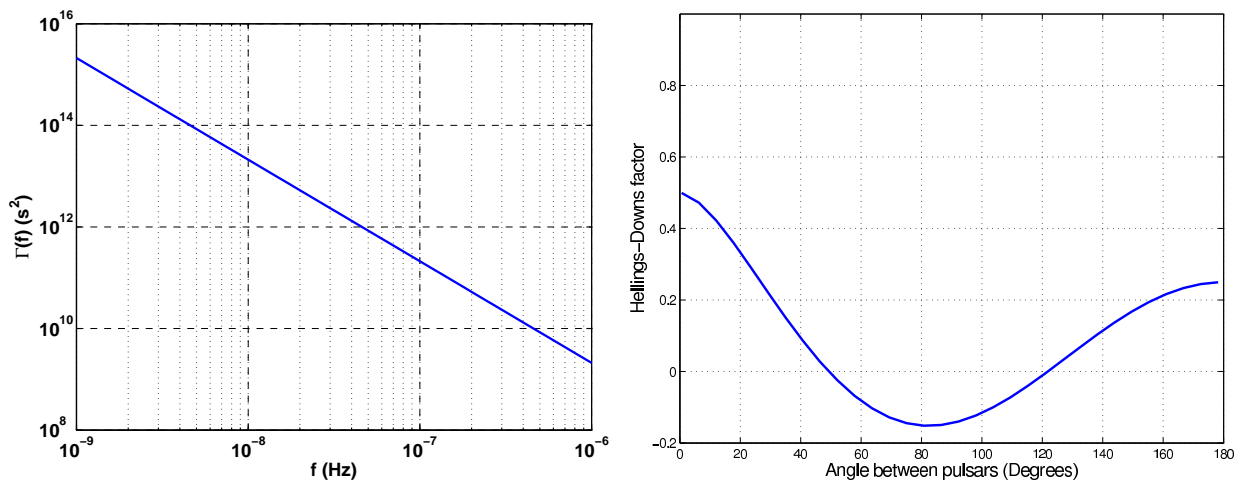


FIG. 6: Left panel: Overlap reduction function for a pair of pulsars, with $\zeta_{IJ}$ chosen to be 0.25. Right panel: Hellings and Downs function $\zeta(\psi_{IJ})$. Note that the overlap reduction function is a function of frequency for a *fixed* pair of pulsars, while the Hellings and Downs function is a function of the angle between two pulsars, and is *independent* of frequency.

2. Assume an observation time $T$, typically between 1 and 10 yr.

3. For a set of power-law indices e.g., $\beta = \{-8, -7, \cdots 7, 8\}$ and some choice of reference frequency $f_{\text{ref}}$, calculate the value of the amplitude $\Omega_\beta$ such that the integrated squared signal-to-noise ratio has some fixed value, e.g., $\rho = 1$. Explicitly,

$$\Omega_\beta = \frac{\rho}{\sqrt{2T}} \left[ \int_{f_{\min}}^{f_{\max}} df \, \frac{(f/f_{\text{ref}})^{2\beta}}{\Omega_{\text{eff}}^2(f)} \right]^{-1/2}, \qquad (29)$$

where $[f_{\min}, f_{\max}]$ define the bandwidth $\Delta f$ of the detectors. Note that the choice of $f_{\text{ref}}$ is arbitrary and will not affect the sensitivity curve.

4. For each pair of values for $\beta$ and $\Omega_\beta$, plot $\Omega_{\text{gw}}(f) = \Omega_\beta (f/f_{\text{ref}})^\beta$ versus $f$.

5. The envelope of the $\Omega_{\text{gw}}(f)$ power-law curves is the power-law integrated sensitivity curve for a correlation measurement using two or more detectors.

*Interpretation*: Any line (on a log-log plot) that is tangent to the power-law integrated sensitivity curve corresponds to a gravitational-wave background power-law spectrum with an integrated squared signal-to-noise ratio $\rho = 1$. This means that if the curve for a predicted background lies *everywhere below* the sensitivity curve, then $\rho < 1$ for such a background. On the other hand, if the curve for a predicted power-law background with spectral index $\beta$ lies *somewhere above* the sensitivity curve, then it will be observed in a correlation measurement with an expected value of $\rho = \Omega_\beta^{\text{pred}}/\Omega_\beta > 1$. Graphically, $\Omega_\beta^{\text{pred}}$

is the value of the predicted power-law spectrum evaluated at $f_{\text{ref}}$, while $\Omega_\beta$ is the value of the same power-law spectrum that is tangent to the sensitivity curve, also evaluated at $f_{\text{ref}}$.

## B.  Plots

The calculation of a power-law integrated sensitivity curve is demonstrated in the left-hand panel of Fig. 7 for the Hanford-Livingston (H1L1) pair of Advanced LIGO detectors. Following steps 1–5 above, we begin with the design detector noise power spectral density $P_n(f)$ for an Advanced LIGO detector [14] (which we assume to be the same for both H1 and L1), and divide by the H1L1 overlap reduction function to obtain the effective strain spectral density $S_{\text{eff}}(f) = P_n(f)/\Gamma_{\text{H1L1}}(f)$ of the detector pair to a gravitational-wave background (see Eq. 23). We then convert $S_{\text{eff}}(f)$ to an energy density $\Omega_{\text{eff}}(f)$ via Eq. 3 to obtain the solid red curve. After integrating 1 yr of coincident data, and assuming a frequency bin width of 0.25 Hz, we obtain the solid green curve, which is lower by a factor of $1/\sqrt{2T\delta f}$. Then assuming different spectral indices $\beta$, we integrate over frequency (see Eq. 29), setting $\rho = 1$ to determine the amplitude $\Omega_\beta$ of a power-law background. This gives us the set of black lines for each power law index $\beta$. The blue power-law integrated curve is the envelope of these black lines.

The right-hand panel of Fig. 7 illustrates how to interpret a power-law integrated sensitivity curve. We replot the green and blue curves from the left-hand panel, which respectively represent the time-integrated and power-law integrated sensitivity of an Advanced LIGO H1L1 correlation measurement to a gravitational-wave background. Additionally, we plot two theoretical spectra of the form $\Omega_{\text{gw}}(f) \propto f^{2/3}$, which is expected for a background due to compact binary coalescences. The dark brown line corresponds to a somewhat pessimistic scenario in which Advanced LIGO, running at design sensitivity, would detect $\approx 10$ individual binary neutron star coalescences per year of science data [13]. The light brown line represents a somewhat optimistic model in which Advanced LIGO, running at design sensitivity, would detect $\approx 100$ individual binary neutron star coalescences per year of science data [13]. (A binary-neutron-star detection rate of $40\,\text{yr}^{-1}$ is considered a realistic rate for Advanced LIGO [15].) The light-brown curve intersects the blue power-law integrated curve, indicating that the somewhat optimistic model will induce a signal-to-noise ratio $\rho > 1$. The dark brown curve falls below the blue power-law integrated curve, indicating that the somewhat pessimistic model will induce a signal-to-noise ratio $\rho < 1$. Note that *neither* curve intersects the green time-integrated sensitivity curve.

In Fig. 9–11 we plot power-law integrated sensitivity curves for several upcoming or proposed experiments: networks of Advanced LIGO detectors, BBO, and a pulsar timing array.

(a) For the Advanced LIGO networks, we use the design detector noise power spectral density $P_n(f)$ taken from [14] assumed to be the same for every detector in the network. We consider three networks: H1L1 (just the US aLIGO detectors), H1H2 (a hypothetical co-located pair of aLIGO detectors), and H1L1V1K1 (the US aLIGO detectors plus detector pairs created with Virgo V1 and KAGRA K1)[3]. In reality, Virgo and KAGRA are expected to have different noise curves than aLIGO, but we assume the same aLIGO noise for each detector in order to show how the sensitivity curve changes by adding additional identical detectors to the network. Given this assumption, the effective strain power spectral density can be written as

$$S_{\text{eff}}(f) = P_n(f)/\mathcal{R}_{\text{eff}}(f)\,, \tag{30}$$

where

$$\mathcal{R}_{\text{eff}}(f) = \left[\sum_{I=1}^{M}\sum_{J>I}^{M}\Gamma_{IJ}^2(f)\right]^{1/2} \tag{31}$$

is the sky- and polarization-averaged response of the network to a gravitational-wave background. A plot of the various overlap reduction functions $\gamma_{IJ}(f)$ and $\mathcal{R}_{\text{eff}}(f)$ for the H1L1V1K1 network are given in Fig. 8. The resulting power-law integrated sensitivity curves are shown in Fig. 9.

(b) For the BBO sensitivity curve, the noise power spectral density for the two Michelson interferometers is taken to be

$$P_n(f) = \frac{4}{L^2}\left[(\widetilde{\delta x})^2 + \frac{(\widetilde{\delta a})^2}{(2\pi f)^4}\right]\,, \tag{32}$$

where

$$(\widetilde{\delta x})^2 = 2 \times 10^{-34}\,\frac{\text{m}^2}{\text{Hz}}\,, \tag{33}$$

$$(\widetilde{\delta a})^2 = 9 \times 10^{-34}\,\frac{\text{m}^2}{\text{s}^4 \cdot \text{Hz}} \tag{34}$$

are the position and acceleration noise (see Table II from [11]) and $L = 5 \times 10^7$ m is the arm length. Following [12], we have included an extra factor of 4 multiplying the first term in Eq. 32, which corresponds to high-frequency noise 4 times larger than shot noise alone. The overlap reduction function for the Michelson interferometers located at opposite vertices of the BBO hexagram is shown in the right panel of Fig. 5. The power-law integrated curve for BBO is given in Fig. 10a.

---

[3] We have taken the location and orientation of the KAGRA detector to be that of the TAMA 300-m interferometer in Tokyo, Japan. We have not included the planned LIGO India detector [16] in this network, as the precise LIGO-India site has not yet been decided upon.
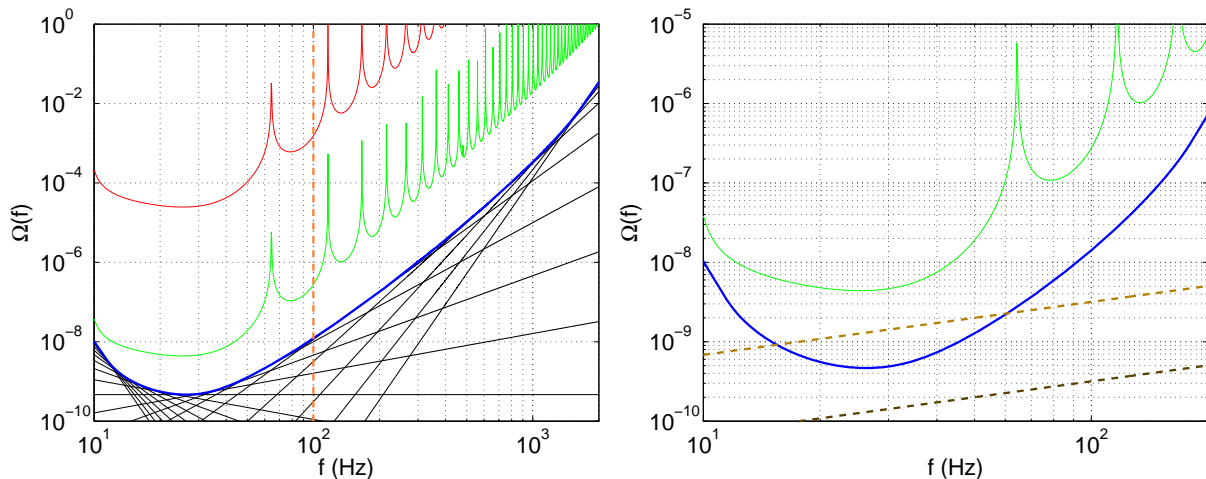
FIG. 7: Left panel: $\Omega_{\mathrm{gw}}(f)$ sensitivity curves from different stages in a potential future Advanced LIGO H1L1 correlation search for power-law gravitational-wave backgrounds. The red line shows the effective strain spectral density $S_{\mathrm{eff}}(f) = P_n(f)/\Gamma_{\mathrm{H1L1}}(f)$ of the H1L1 detector pair to a gravitational-wave background signal converted to energy density $\Omega_{\mathrm{eff}}(f)$ via Eq. 3. (The $P_n(f)$ used in this calculation is the design detector noise power spectral density for an Advanced LIGO detector, assumed to be the same for both H1 and L1.) The spikes in the red curve are due to zeroes in the overlap reduction function $\Gamma_{\mathrm{H1L1}}(f)$, which is shown in the left panel of Fig. 5. The green curve, $S_{\mathrm{eff}}(f)/\sqrt{2T\delta f}$, is obtained through the optimal combination of one year's worth of data, assuming a frequency bin width of $0.25\,\mathrm{Hz}$ as is typical [2]. The vertical dashed orange line marks a typical Advanced LIGO reference frequency, $f_{\mathrm{ref}} = 100\,\mathrm{Hz}$. The set of black lines are obtained by performing the integration in Eq. 29 for different power law indices $\beta$, requiring that $\rho = 1$ to determine $\Omega_\beta$. Finally, the blue power-law integrated sensitivity curve is the envelope of the black lines. Right panel: a demonstration of how to interpret a power-law integrated curve. The thin green line and thick blue line are the same as in the left panel. The two dashed brown lines represent two different plausible signal models for gravitational-wave backgrounds arising from binary neutron star coalescence; see, e.g., [13]. In each case, $\Omega_{\mathrm{gw}}(f) \propto f^{2/3}$; however, the two curves differ by an order of magnitude in the overall normalization of $\Omega_{\mathrm{gw}}(f)$. The louder signal will induce a signal-to-noise-ratio $\rho > 1$ with an Advanced LIGO H1L1 correlation measurement as it intersects the blue power-law integrated curve—even though it falls below the time-integrated green curve. The weaker signal will induce a signal-to-noise-ratio $\rho < 1$ with Advanced LIGO H1L1 as it is everywhere below the power-law integrated curve.
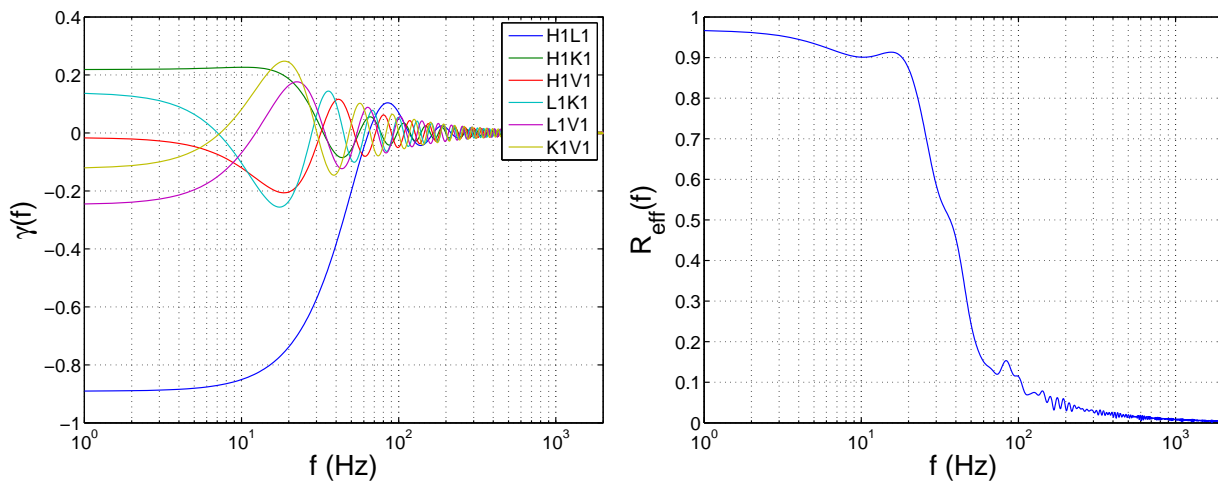


FIG. 8: Left panel: Individual normalized overlap reduction functions for the six different detector pairs comprising the H1L1K1V1 network. Right panel: Sky- and polarization-averaged reponse of the H1L1V1K1 network to a gravitational-wave background.

(c) For the pulsar timing array sensitivity curve, we consider a network of 20 pulsars taken from the International Pulsar Timing Network (IPTA) [17], which we assume have identical white timing noise power spectral densities,

$$P_n(f) = 2\Delta t\,\sigma^2\,, \qquad (35)$$

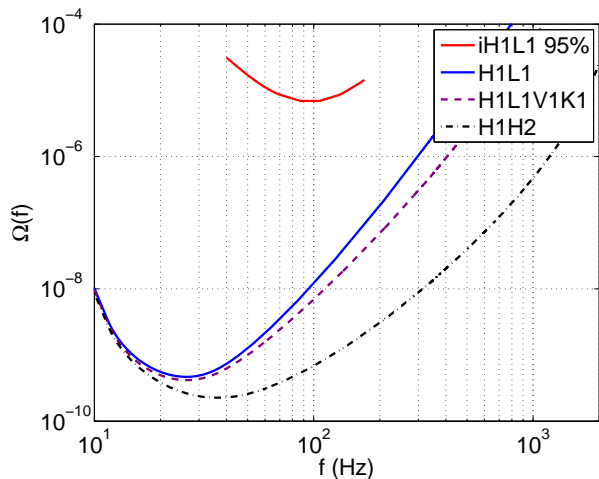where $1/\Delta t$ is the cadence of the measurements, taken to

FIG. 9: Different networks of advanced detectors assuming $T = 1\,\mathrm{yr}$ of observation. We also include 95% CL limits from initial LIGO for comparison [2].

be 20 $\mathrm{yr}^{-1}$, and $\sigma$ is the root-mean-square timing noise, taken to be 100 ns. We note that the pulsar timing network we envision may be somewhat optimistic as 100 ns root-mean-square timing noise is ambitious. Also, we do not include the loss of sensitivity arising from the fitting of each pulsar's period $P$ and spin-down rate $\dot{P}$.

Since the timing noise power spectral densitites are identical, it follows that

$$S_{\mathrm{eff}}(f) = S_n(f) \left[ \sum_{I=1}^{M} \sum_{J>I}^{M} \zeta_{IJ}^2 \right]^{-1/2}, \qquad (36)$$

where

$$S_n(f) = P_n(f)/\mathcal{R}(f) = 12\pi^2 f^2 \, P_n(f) \qquad (37)$$

and $\zeta_{IJ}$ are the Hellings and Downs factors for each pair of pulsars in the array. For our choice of 20 pulsars,

$$\sum_{I=1}^{M} \sum_{J>I}^{M} \zeta_{IJ}^2 = 4.7379 \,, \qquad (38)$$

which can thought of as the *effective* number of pulsar pairs for the network. Finally, we assume a total observation time $T = 5$ yr, which sets the lower frequency limit of $S_{\mathrm{eff}}(f)$. Given these parameters, we expect the pulsar timing array to be operating in the "intermediate signal limit" [18]. We therefore utilize the scaling laws from Fig. 2 in Ref. [18] to adjust the power-law integrated curves, since Eqs. 21, 22 for $\rho$ are valid in the *weak-signal limit* and overestimate the expected squared signal-to-noise ratio by a factor of $\approx 5$ for an observation of $T = 5$ yr. The power-law integrated curve for IPTA is given in Fig. 10b.

It is interesting to note that the power-law integrated curves for Advanced LIGO and BBO are relatively round

in shape, whereas the pulsar timing curve is pointy. This reflects the fact that the sensitivity of pular timing measurements is mostly determined by a small band of the lowest frequencies in the observing band regardless of the spectral shape of the signal.

(d) Finally, Fig. 11 shows the power-law integrated sensitivity curves for the different detectors on a single plot spanning a wide range of frequencies.

## IV. DISCUSSION

We have presented a graphical representation of detector sensitivity curves for power-law gravitational-wave backgrounds that takes into account the enhancement in sensitivity that comes from integrating over frequency in addition to integrating over time. We applied this method to construct new power-law integrated sensitivity curves for cross-correlation searches involving advanced ground-based detectors, BBO, and a network of pulsars from a pulsar timing array. The new curves paint a more accurate picture of the expected sensitivity of upcoming observations. The code that we used to produce the new curves is available at `https://dcc.ligo.org/LIGO-P1300115` for public download. Hopefully, this will allow other researchers to easily construct similar sensitivity curves for their analyses. Required inputs are the noise power spectral density $P_{nI}(f)$ for each detector in the network and the overlap reduction function $\Gamma_{IJ}(f)$ for each detector pair. Common default files are available for download with the plotting code.

Although the above discussion has focused on comparing predicted strengths of gravitational-wave backgrounds to sensitivity curves for current or planned detectors, one can also present measured upper limits for power-law backgrounds in a similar way. That is, instead of plotting the upper limits for $\Omega_\beta$ (for fixed $f_{\mathrm{ref}}$) as a function of the spectral index $\beta$ as in [2, 19, 20], one can plot the envelope of upper-limit power-law curves as a function of frequency. This would better illustrate the frequency dependence of the upper limits in the observing band of the detectors.
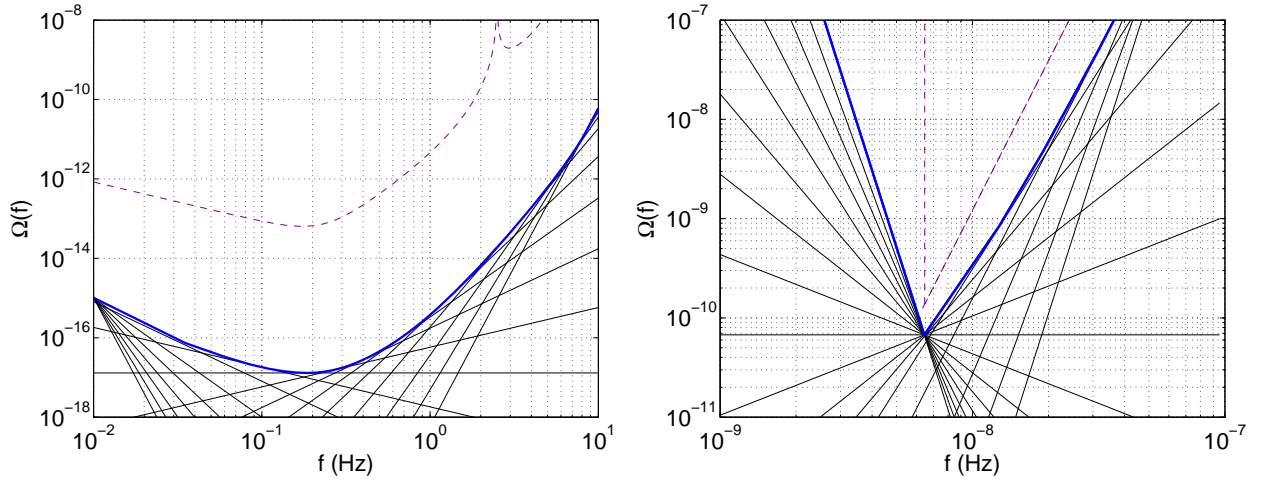
FIG. 10: One-sigma, power-law integrated sensitivity curves. The dashed purple curves show the effective strain spectral density $S_{\rm eff}(f)$ converted to energy density $\Omega_{\rm eff}(f)$ (see Eqs. 23, 3). Left panel: BBO assuming $T = 1\,{\rm yr}$ of observation. The spike at $\approx 2.5\,{\rm Hz}$ is due to a zero in the BBO overlap reduction function. Right panel: A pulsar timing array consisting of 20 pulsars, $100\,{\rm ns}$ timing noise, $T = 5\,{\rm yr}$ of observation, and a cadence of $20\,{\rm yr}^{-1}$.
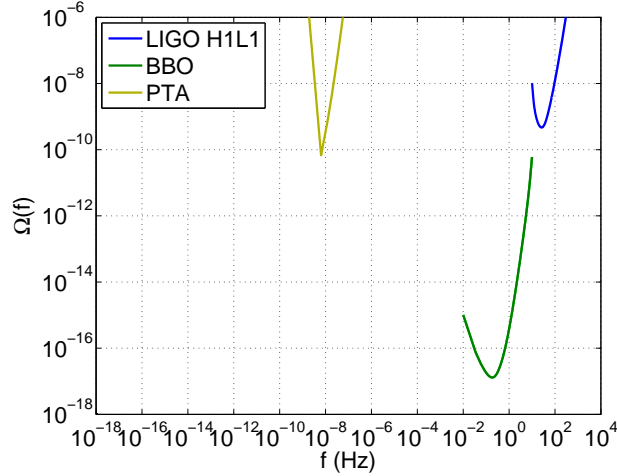


FIG. 11: Power-law integrated sensitivity curves for different detectors plotted over a wide range of frequencies.

[1] G. Hobbs, in *High-Energy Emission from Pulsars and their Systems*, edited by D. F. Torres and N. Rea (Springer Berlin Heidelberg, 2011), Astrophysics and Space Science Proceedings, p. 229.

[2] B. Abbott et al., Nature **460**, 990 (2009).

[3] B. Allen and J. Romano, Phys. Rev. D **59**, 102001 (1999).

[4] N. Christensen, Physical Review D **46**, 5250 (1992).

[5] É. É. Flanagan, Physical Review D **48**, 2389 (1993).

[6] N. J. Cornish and S. L. Larson, Class. Quantum Grav. **18**, 3473 (2001).

[7] L. S. Finn, S. L. Larson, and J. D. Romano, Phys. Rev. D **79**, 062003 (2009).

[8] R. W. Hellings and G. S. Downs, Astrophys. J. Lett. **265**, L39 (1983).

[9] M. Anholm, Phys. Rev. D **79**, 084030 (2009).

[10] S. Phinney et al., NASA Mission Concept Study (2004).

[11] J. Crowder and N. J. Cornish, Phys. Rev. D **72**, 083005 (2005).

[12] C. Cutler and J. Harms, Phys. Rev. D **73**, 042001 (2006).

[13] C. Wu, V. Mandic, and T. Regimbau, Phys. Rev. D **85**, 104024 (2012).

[14] D. Shoemaker, *Advanced ligo anticipated sensitivity curves* (2010), URL https://dcc.ligo.org/LIGO-T0900288/public.

[15] J. Abadie et al., Class. Quantum Grav. **27**, 173001 (2010).

[16] B. Iyer et al., *LIGO-India Tech. Rep.* (2011), URL `https://dcc.ligo.org/cgi-bin/DocDB/ShowDocument?docid=75988`.

[17] G. Hobbs et al., Class. Quantum Grav. **27**, 084013 (2010).

[18] X. Siemens, J. Ellis, F. Jenet, and J. D. Romano (2013), `http://arxiv.org/abs/1305.3196`.

[19] J. Abadie et al., Phys. Rev. D **85**, 122001 (2012).

[20] V. Mandic, E. Thrane, S. Giampanis, and T. Regimbau, Phys. Rev. Lett. **109**, 171102 (2012).